IMPORTANT LESSONS FROM FIELD RECONNAISSANCE FOLLOWING THE 2016 MEINONG EARTHQUAKE IN SOUTHERN TAIWAN

T.C. Hutchinson[1], K. Clahan[2], J. Sun[3], F. Menq[4], E. Lo[1], W.-J. Chang[5], C.-C. Tsai[6]

[1] *University of California, San Diego (UCSD), tara@ucsd.edu and eklo@eng.ucsd.edu*
[2] *Lettis Consultants International (LCI), clahan@lettisci.com*
[3] *Pacific Gas & Electric (PG&E), JIS4@pge.com*
[4] *University of Texas, Austin (UTA), fymenq@utexas.edu*
[5] *National Cheng Kung University (NCKU), wjchang@mail.ncku.edu.tw*
[6] *National Chung Hsing University, (NCHU), tsaicc@dragon.nchu.edu.tw*

Abstract

The M_w 6.3 Meinong earthquake, which struck southern Taiwan on February 6, 2016, was characterized by an oblique left lateral strike-slip motion with a minor reverse component. The earthquake occurred at approximately 16 km depth on an unknown fault that did not rupture the ground surface, but rather produced a noticeable long period velocity pulse east to west, with the strongest amplitude motions recorded about 30km west of the epicentral region in Tainan City. Within this city, more than 20 multi-story buildings constructed under relatively modern building codes were severely damaged, including seven that suffered complete collapse. In addition, there was widespread damage associated with liquefaction, a substantial portion of which affected residential buildings causing large uniform and differential settlement, the later causing severe tilt to buildings in many cases. In response to this event, local earthquake professionals, faculty members, and students teamed with US NSF-sponsored Geotechnical Extreme Events Reconnaissance (GEER) members visited the affected area to document the geologic/geotechnical effects and to assess seismic performance of infrastructure [1,2]. Unique to past efforts, US-Taiwan reconnaissance team members utilized unmanned aerial vehicles and LiDAR in several areas to guide the field data collection efforts and assist with post-reconnaissance data interpretation. This paper presents important lessons learned from this event, focusing particularly on 1) the impact of marginally liquefiable soils on shallow foundations and in particular foundation detailing aspects which led to good performance and 2) the advantages of using remote sensing tools to offer insight into important features of earthquake performance post-event.

Keywords: earthquake reconnaissance, liquefaction, foundations, remote sensing, unmanned aerial vehicles;

1. Introduction

1.1 Geology and Unique Fault Features

The February 6, 2016, M_w 6.3 Meinong earthquake occurred in southwest Taiwan near the major cities of Tainan, Chiayi, and Kaohsiung, which sustained significant damage. Southwest Taiwan is an area with a high rate of West-Southwest crustal shortening and associated seismicity resulting from the oblique convergence of the Philippine Sea Plate and Eurasian Plate. Since 2000, 12 $M_L \geq 6.0$ earthquakes have occurred beneath the island of Taiwan. The recent Meinong earthquake produced significant damage to nearby cities, especially when compared to other $M_L \geq 6.0$ inland earthquakes, which typically produced only minor damage. Historically, there have been 22 damaging earthquakes in Taiwan during the last century. The most destructive have been the April 21, 1935 M=7.1 Hsinchu-Taichung earthquake and the September 12, 1999 M = 7.3 Chi-Chi earthquake, which resulted in more than 3200 and 2400 deaths, respectively. The $M_L \geq 6.0$ earthquakes that are occurring in southwest Taiwan including the February 6, 2016, Meinong earthquake, are typically located at moderate depths ranging between 12 and 27 km on developing faults that are "blind" and do not reach the ground surface but are often manifested as folds that uplift the ground surface as part of the western fold and thrust belt.

The Quaternary geomorphology of the Tainan area reflects the cyclic behavior and subsequent uplift of the nearshore marine environment (Figure 1). The history of accretion and uplift as recorded in the stratigraphy of the Tainan area can be divided into four stages: (1) deposition of Miocene to Pleistocene continental slope fine to coarser grained marine deposits which consist of intercalated sandstones and shales and is located within the western portion of the Western Foothills; (2) deposition of the Holocene, shallow marine Tainan Fm sandstone which is reportedly on the order of up to 200 m thick; (3) deposition of Holocene marine terrace deposits along the margin of the Western Foothills; and (4) deposition of the shallow Dawan marine estuarine deposits consisting of fine sand and silts which are reportedly between 2750 and 300 years old and locally on the order of 20 to 40 m thick. The Holocene Tainan and Dawan Fms underlie areas of moderate and high liquefaction potential in the Tainan area, respectively. The majority of collapsed buildings, damaged buildings, and buildings affected by liquefaction are primarily located within the loose fine sand and silt deposits of the Dawan Fm.
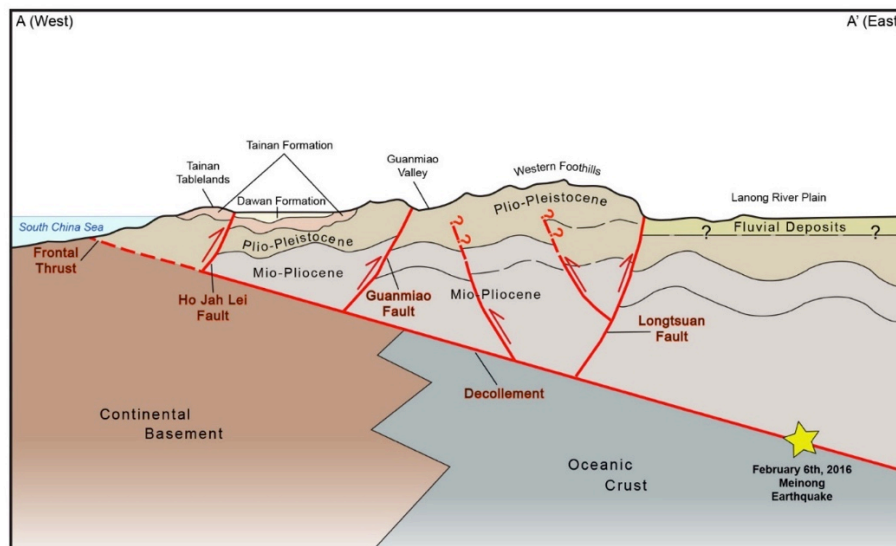

Fig. 1 - Schematic cross section, E-W across southern Taiwan (see Figure 2 for cross section location).

No conclusive evidence of surface rupture from the Meinong earthquake emerged, nor was any reported along any geologic structures in southwest Taiwan. However, Interferometric Synthetic Aperture Radar (InSAR) data supplied by the JPL-Caltech Advanced Rapid Imaging and Analysis (ARIA) project provided important evidence for vertical ground displacement associated with the Meinong earthquake. The InSAR data show vertical displacement and uplift of over 12 cm across the Western Foothills as well as distinct uplift of over 10

cm within the Guanmiao Hills west of the Guanmiao Valley (Figure 2). A sharp N-S trending displacement lineament separating the area of uplift (Guanmiao Hills) and the down-dropped Guanmiao Valley shows up very clearly on the InSAR imagery. This sharp displacement lineament appears to delineate a west-dipping, N-S trending fault approximately 10 km long along the western margin of the Guanmiao Valley (Figure 2). UAV imagery contributed to a 3-D digital elevation model (DEM) to more accurately examine the geomorphic and geologic characteristics along this sharp geomorphic lineament (scarp) and determine that the uplift is likely fault rather than fold related. This feature, which has now been labeled the Guanmiao Fault, may have uplifted as part of triggered slip from either the mainshock of the 2016 Meinong earthquake or a possible second event that occurred seconds later and appears to be more closely located near the Guanmiao fault at depth. Movement along the west dipping Guanmiao fault would place part of Tainan (the eastern area comprised of the Dawan lowlands) on the hanging wall. In theory, this potential second event and movement along the Guanmiao fault may possibly explain the increased levels of earthquake effects and damage in nearby Tainan City.
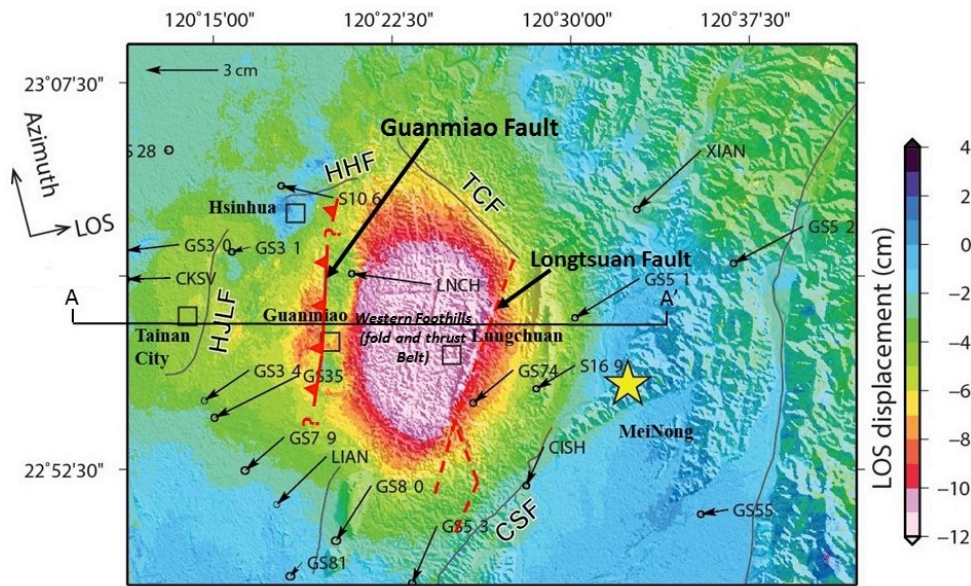

Fig. 2 - Interpreted InSAR image showing the Guanmiao fault and uplift of the Western Foothills Fold and Thrust Belt; see Figure 2 for cross section (courtesy of M. H. Huang and JPL-Caltech Advanced Rapid Imaging and Analysis [ARIA] project); the Sentinel-1 image contain Copernicus data.

1.2 Intensity of Ground Shaking

About a third of Taiwan experienced an intensity V shaking during this event, while the highest intensity VI occured in Tainan city. A total of just over 50 real-time data stations operated by the Taiwan Central Weather Bureau (CWB) were triggered by the earthquake. Near the epicenter, five stations within a radius of 35 km from the epicenter recorded a peak ground acceleration (PGA) at or below 0.1g., while intensity increased to a PGA of about 0.25g in Tainan City. The largest PGA recorded for this event was 0.41g at a distance of 25km from the epicenter (Figure 3). A noted feature for this earthquake is a long period velocity pulse that was observed in many stations near Tainan City. For example, Figure 4 shows the velocity waveforms of the Palert station W21B, which articulates a distinct long period velocity pulse with a peak ground velocity (PGV) of about 1 m/sec. Palert is the instrument implemented for earthquake early warning (EEW). While these instruments are not on a free-field, they are installed on the 1st or 2nd floor of elementary schools [3]. Despite the non-free field and low cost of Palert stations, these stations provide instant real-time records to give the first glimpse of the waveforms as the observation of the 1-sec velocity pulse, which might be the main cause of the damage in Tainan.
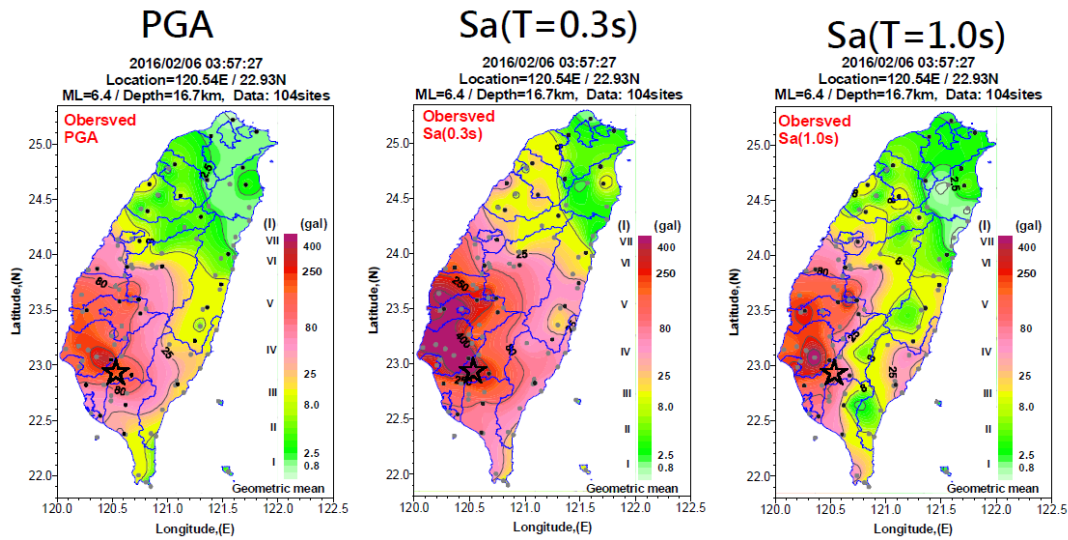
Fig. 3 - Recorded peak and spectral accelerations during the Meinong Earthquake (estimated by NCREE using CWB data sources)
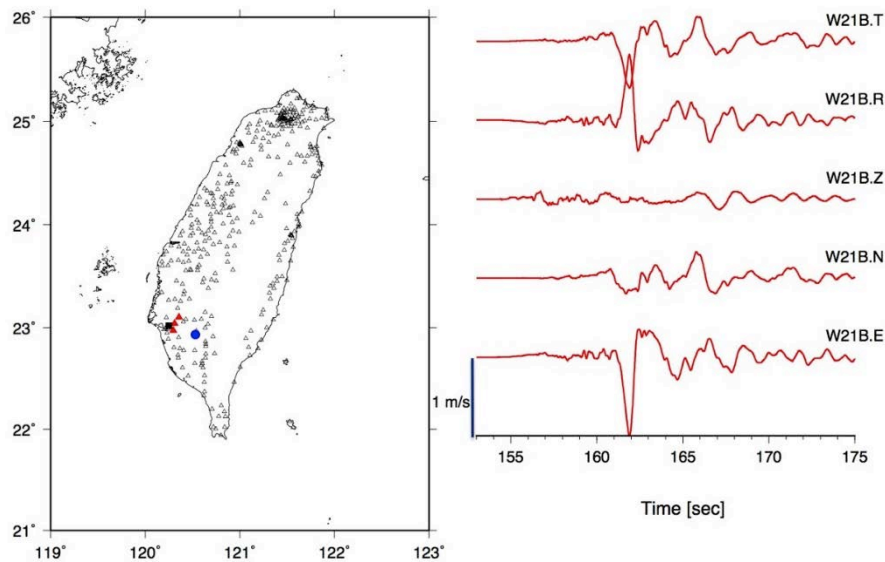

Fig. 4 - Earthquake Early Warning (EEW), Palert instrument and station distribution, and the velocity waveforms at station W21B.

2. Liquefaction-Induced Damage

2.1 Overview

The sites that experienced liquefaction in the Meinong earthquake around Tainan can be grouped into three categories: (1) liquefaction developed in residential areas where ground liquefaction occurred in maturely developed sectors of the city, (2) liquefaction developed in open fields where surface manifestation is not obstructed by manmade improvements, and (3) liquefaction triggered lateral spreading along river banks. This paper focuses on the geotechnical, foundation, and building performance aspect of sites where liquefaction occured in developed residential areas (Figure 5a). One specific site (Annan, Figure 5b) is highlighted in extensive detail to offer a summary of key findings in this regard, while interested readers may find additional sites summarized in the teams reconnaissance report [1]. The specific Annan site discussed herein is located in the Dinshi community of Annan district, Tainan city. Based on the distribution of sand boils and building

4

settlement, the zone of liquefaction of the Annan site is outlined in Figure 5b. Overlapping the current and the 1898 maps, clearly indicates that the liquefaction occurred in the area mapped as an old fish pond, with the two sides of the liquefied boundaries located along the mapped old dike. Field reconnaissance identified differential settlement along the dike as high as 50 cm in some locations. Typical failure patterns included ground settlements, cracks of pavements, settlement/tilting of reinforced concrete structures on shallow foundations, and rupture of underground utilities.

(a)   (b)
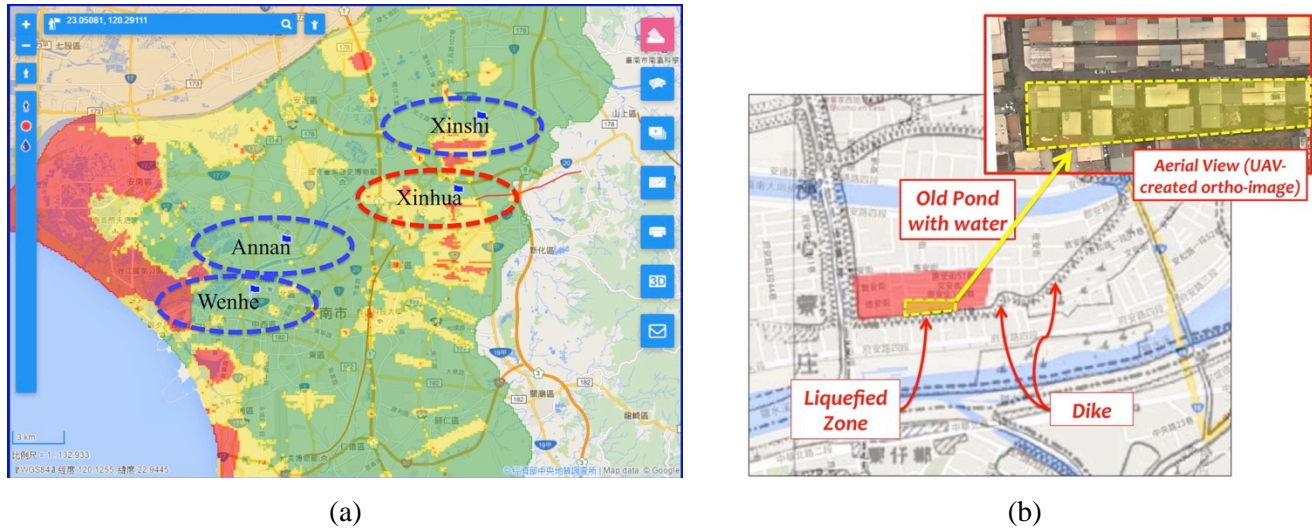
Fig. 5 – (a) Survey sites near Tainan City where extensive liquefaction was observed (note that Annan, Wenhe, and Xinshi are residential areas, while Xinhua is an open area and region of repeated liquefaction, see [1]). A recent liquefaction hazard map is offered in the background (background map courtesy of [7]), where green, yellow, and red = low, medium, and high liquefaction potential, respectively. (b) Overlap of 1898 map [8] and present-day Google map at the Annan site (inset denotes location of region presented in damage mapping in Figure 7) (1898 map source [8])

2.2 Properties of Liquefied Soils and Vs Profiles

Samples of ejected material were taken at all four sites where extensive liquefaction was observed (Figure 5a) and tested for their physical properties. Table 3 summarizes the grain size, plasticity, and USCS soil classification. Test results indicate that the ejected materials are predominantly poorly-graded fine sands (SP) and silty fine sands (SM) with fine contents ranging from 6 to 30%. Grain size distribution curves indicate that the ejected soils all have very uniform gradation with C_u (= D60/D10) varying between 1 to 3, especially between the 80% and 20% passing range where the curves show very steep slopes. It is recognized that some fines may have been lost during the ejection process, and thus the reported fines may be less than the in-place soils before they were ejected.

Table 3. General properties of ejected soils (the Annan site is discussed herein)

Site	Gravel (%)	Sand (%)	Fines (%)	LL	PI	USCS
Annan	0	75	25	--	NP	SM
Wenhe	0	81	19	26	NP	SM
Xinshi	0	94	6	--	NP	SP
Xinhua	0	70	30	--	NP	SM

By comparing the liquefied residential sites with the historical pre-development map prepared in 1898, each of the sites surveyed were noted to be located in areas previously mapped as fish ponds (e.g. Figure 5b). These ponds were backfilled in the 1970s to 1980s during a rapid economic growth period of Taiwan. It is also notable that the ponds were backfilled at different times, by different developers, and thus likely using different construction means and materials. While it might be anticipated that during strong shaking each of these sites may liquefy due to their poor quality, the seismic performance of individual backfilled ponds is expected to behave differently during moderate ground shaking. The reduced quality of backfill of these fish ponds is likely responsible for the liquefaction in the residential areas. The areas that experienced liquefaction during the Meinong earthquake are generally isolated and limited to areas less than 0.05 km^2.

An emerging issue recognized during this reconnaissance is the need to identify potential local liquefiable zones in residential areas. While available geologic and historical planning maps are both good references to help identify potential liquefaction areas, they are not accurate enough to describe the liquefaction potential at a small enough scale for an individual property owner (Figure 5 clearly demonstrates this). Based on observations from this earthquake reconnaissance, Vs profiling techniques (multi-channel analysis of surface waves; MASW) provides good data for estimating liquefaction potential. Herein, the simplified procedure using V_s data generated through MASW [6] is used to identify the liquefied layer. These results show that the liquefied layers are located at depths of 2 to 6 m below grade, which is the general depth of commercial fish ponds in this area and corresponds to the depth ranges of the loose backfill (Figure 6). This is also in agreement with observations in the field that new buildings constructed with a deeper basement performed well in areas where adjacent older structures without a basement suffered liquefaction induced settlement and associated structural distress. An example is shown for the Annan area, where MASW surveys conducted on February 24, 2016 (2.5 weeks after the event), provide the V_s profiles measured near a severely damaged building (Figure 10). Note that the ground water table is estimated at the depth of 2.3 m below the surface; as inferred from the Vs profile and confirmed by local residents. Results of the liquefaction analysis indicate that the liquefied layer is located at depths from 2.3 to 6 m (Figure 6). Moreover, the non-liquefied zones have an ample factor of safety over 2.5 at all depths. These results agree with the performance of subsoils during this event and the history of the site.
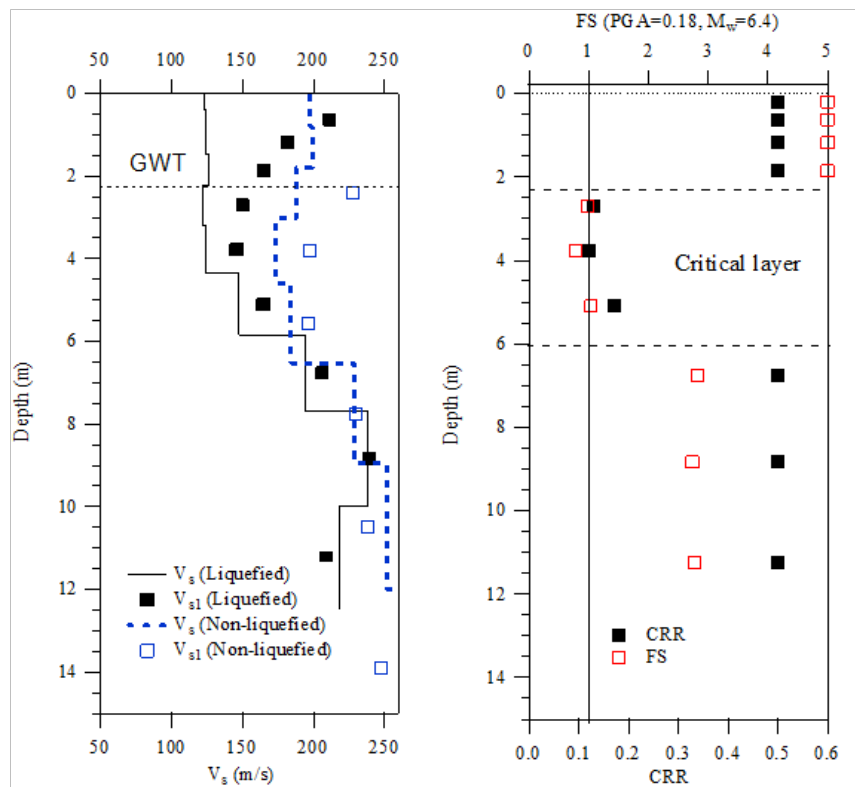

Fig. 6 – Annan district Vs profiles and liquefaction triggering estimates.

2.3 Liquefaction-induced Damage to Buildings and Correlation with Ground Failure

Assessment of ground failure at the residential sites were evaluated using the Ground Failure Index presented in Table 1; while assessment of structural damage utilized the indices presented in Table 2. Figure 7 adapts the ground failure-structural damage mapping of Tables 1 and 2 with a simple color-coding overlaid on individual buildings in a local region most heavily damaged within Annan. This map is useful as it provides context to the extent of ground failure as contextualized with foundation damage and its link with physical damage state of buildings in the region. To interpret the map, note that ground failure is delineated via color-coding of the border of individual buildings; while structural damage is delineated via color-coding of the fill used within the building outline.

Table 1 - Ground Failure Index (after [4])

Index	Description	Interpretation
GF0	No Observable Ground Failure	No settlement, tilt, lateral movement, or sediment ejecta
GF1	Minor Ground Failure	Settlement, D < 10 cm; Tilt < 1 degree; no lateral movements
GF2	Moderate Ground Failure	10 cm < D < 25 cm; Tilt of 1-3 degrees; small lateral movements (< 10 cm)
GF3	Significant Ground Failure	D > 25 cm; Tilt of > 3 degrees; Lateral movement > 25 cm

Table 2 - Structural damage index (modified from [5], and as used by [4])

Index	Description	Interpretation
D0	No Observable Damage	No cracking, broken glass, etc.
D1	Light damage	Cosmetic cracking, no observable distress to load-bearing structural elements
D2	Moderate Damage	Cracking in load-bearing elements, but no significant displacements across these cracks
D3	Heavy Damage	Cracking in load-bearing elements with significant deformations across the cracks
D4	Partial Collapse	Collapse of a portion of the building in plan view (i.e., a corner or a wing of the building)
D5	Collapse	Collapse of the complete structure or loss of a floor

Several important aspects can be investigated in the context of Figure 7. Beginning with the highly dominant blue shading at the exterior buildings, these long buildings consistently observe little to no structural damage as graded with a structural damage index between D0 and D1; despite the presence of ground failure features, though graded as minor GF1. The pair of photos shown in Figure 8 articulates an example of a nominal ground failure graded as GF1, where settlement of the structure is observed; yet at most damage to the structure is only cosmetic in nature (graded as D1); despite the manifestation of settlement, the lack of significant structural damage is likely due to the well connected and continuous foundation of this building. Moreover, no building extensions were noted in these buildings. In contrast, Figure 9 provides a perspective view from the south east (viewpoint B in Figure 7) looking onto several buildings where clear evidence of liquefaction in the field is noted as visible in the bulging of exterior slabs (center of image) and rotation of light-weight screen fences (left of image), surface sand boils (in field and elsewhere). The pair of buildings on the left of this image observed ground failure features at their exterior classified as moderate to severe (GF2-GF3; while their resulting structural damage was graded as heavy (D3; significant damage to load bearing elements); as is evident

from views on the opposing side (not shown here); in stark contrast, the long building on the right likely of similar weight and with surrounding ground failure characterized as minor, observed only very minor cosmetic damage. Its foundation and structural system were continuous and no additions were observed along the exterior of this building, which may be why this building suffered no damage despite the visible surrounding ground failure. The most severe ground failure-structural damage locations mapped in Figure 7 are those structures observed from viewpoint C of Figure 7. Graded as yellow through red or D3->D5, these excessive structural damage regions of the district were mostly associated buildings with structural discontinuities primarily at the foundation, and often associated with light-weight single story addition regions (Figure 10).

Fig. 7 – Assessment of ground failure – structural damage index (A, B, C denote images shown in Figures 8, 9, and 10 respectively). (center of region at: 23.0254°, 120.2074°)

Fig. 8 – Example of mapping GF1-D0 (or GF1-D1). (23.0255°, 120.2078°)

Fig. 9 – Example of mapping GF1 through GF3; demonstrating various structural damage states. (23.0254°, 120.2075°)

Fig. 10 – Example of mapping worse case ground and structural damage combination (GF3-DF5). (23.0254°, 120.2074°; Lane 161, Hui'an St)

2.4 Foundation Continuity

A common theme in this and others regions impacted by liquefaction during this event is that perimeter footings, if continually connected, performed well even though the building experienced significant differential movement as manifest in observations of the surrounding soils and hardscape features. In contrast, unreinforced slabs not

tied to the foundation heaved and suffered complete disconnection in most cases in response to surrounding liquefaction (e.g. Figure 11a). Perimeter footings connected with adequately reinforced grade beams generally performed well, even with structures that experienced significant displacement. In some cases, although the ground heaved excessively, no structural cracks were observed within the interior walls of buildings, if sufficient foundation continuity was offered. In these situation, settlement of the building was fairly uniform, rendering very little to no differential displacement onto the structure. Meanwhile ejected sand was observed along slab edges. In fact, light-weight single story extensions to residential buildings almost exclusively suffered severe damage or complete collapse if surrounding liquefaction occured and their foundations were not well integrated (tied to) the primary buildings foundation. In this case, ground heave overcomes the isolated footings limited resistance (e.g. Figure 11b). It was also noted that, while just using the strip footing with sufficient continuity may protect the structural integrity, special attention should be given to the location of the mass center relative to the footing center to prevent tilting should liquefaction (especially uneven liquefaction) occur below the foundation.

(a)   (b)

Fig. 11 – Examples of single story additions, lacking interconected footings with the primary structure: (a) Annan site and (b) Xinshi site (not the structural hinge mechanism that develops within the single story carport beams due to excessive differential settlement of the isolated column footings; the main multi-story structure in the background remained undamaged, whereas the single-story carport was demolished.

3. Remote Sensing Data and Models

3.1 Tools and Techniques

To create 3D models of sites damaged by the 2016 South Taiwan Earthquake, during this reconnaissance, the team employed two unique pieces of remote sensing equipment, namely: 1) a FARO Focus3D S 120 LiDAR scanner and 2) a DJI Phantom 3 Professional quadcopter. The former was utilized primarily to obtain ground-based models of interior or exterior regions of damage patterns (buildings, ground features, etc.). The latter was primarily utilized to obtain high-resolution aerial photographs and generate 3D models of larger spatial extents. Both of these tools are comparatively low cost and lightweight, and therefore ideal for a mobile reconnaissance. The methods used to post-process data collected during these surveys are discussed in prior efforts of the team (e.g. [9,10]). In total, 11 unique sites were surveyed using the remote sensing equipment during a four-day period following the main event. These surveys generated more than 22 GBytes of raw data, including over 3200

high-resolution images via the UAV and 39 discrete LiDAR scans. Uniquely, 3D models (both fly-through videos and interactive 3D models) were embedded in a stand-alone report for future reconnaissance teams to preview prior to their site visit [2]. Specifically, the FARO LiDAR was employed to capture localized features visible from the ground, such as cracks in levees, ground failures, or structural deformations (see e.g. Figure 12). The FARO unit utilized for these surveys has a theoretical range of 120m and accuracy of +/-2mm. Moreover, with an onboard camera, images can be collected in conjunction with laser scan data and texture mapped onto the point cloud during processing. In this effort, when not all features were visible from one viewpoint, multiple overlapping scans were acquired and combined using FARO SCENE 5.5 [11].

The DJI copter was used to acquire images from vantage points, which would be difficult or impossible to otherwise access. The model copter used in this survey was very lightweight at only 1200g and with a diagonal size of 590mm. It is rated for a horizontal speed of 16m/s and vertical speed of 5m/s. On-board the copter is a self-contained 12Megapixel camera with a 94 degree field of view. The team brought four fully charged batteries during each survey day allowing about 80 minutes of flight time. Images collected during the copter flights were processed through Agisoft Photoscan Professional 1.2.3 [12] to create both 3D models as well as high-resolution ortho-photos [2]. UAV photogrammetry datasets were also processed in [12], yielding either a high-resolution ortho-photo, or a 3D model or point cloud. As the images from the DJI Phantom are geotagged, Photoscan is able to geo-reference the model without requirement for ground control points, though control points are used in some sites for validation. Orthophotos were exported in GeoTIFF format for use with QGIS, where they could be analyzed with measurement and annotation, all at full resolution (typically ~2cm/pixel). Low-resolution 3D models were created in 3D PDF format for ease of preview and navigation [2].
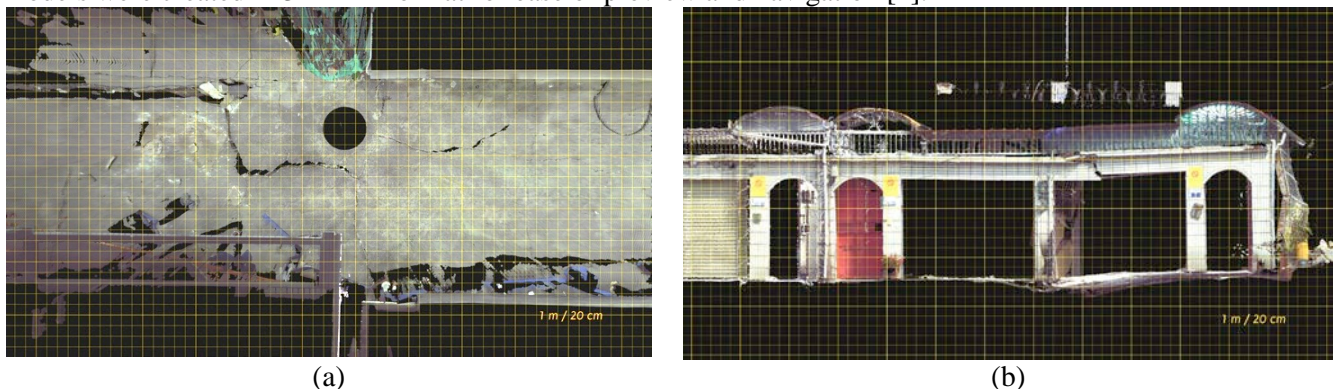

| (a) | (b) |

Figure 12. LiDAR orthographic views overlaid with a 20cm grid: (a) top down view articulating the ground surface cracks in between buildings in Annan (view C in Figure 7), and (b) front view of the residential complex at Xinshi (single story region of Figure 11d).

4. Conclusions

The M_w 6.3 Meinong earthquake, which struck southern Taiwan on February 6, 2016, was characterized by an oblique left lateral strike-slip motion with a minor reverse component. The earthquake occurred at approximately 16 km depth on an unknown fault that did not rupture the ground surface, but rather produced a noticeable long period velocity pulse east to west, with the strongest amplitude motions recorded about 30km west of the epicentral region in Tainan City. Within this city, more than 20 multi-story buildings constructed under relatively modern building codes were severely damaged, including seven that suffered complete collapse. In addition, there was widespread damage associated with liquefaction, a substantial portion of which affected residential buildings causing large uniform and differential settlement, the later causing severe tilt to buildings in many cases. In response to this event, local earthquake professionals, faculty members, and students teamed with US NSF-sponsored Geotechnical Extreme Events Reconnaissance (GEER) members and visited the affected area to document the geologic/geotechnical effects and to assess seismic performance of infrastructure. Unique to past efforts, US-Taiwan reconnaissance team members utilized unmanned aerial vehicles and LiDAR in several areas to guide the field data collection efforts and assist with post-reconnaissance data interpretation. This paper presents important lessons learned from this event, focusing particularly on 1) the impact of

marginally liquefiable soils on shallow foundations and in particular foundation detailing aspects which led to good performance and 2) the advantages of using remote sensing tools to offer insight into important features of earthquake performance post-event.

4. Acknowledgements

5. References

[1] Sun, J., Hutchinson, T.C., Clahan, K., Menq, F., Lo, E., Chang, W.-J., Tsai, C.-C., Ma, K.-F. (2016a). Geotechnical Reconnaissance of the 2016 Mw 6.3 Meinong Earthquake, Taiwan. A report of the NSF- Sponsored GEER Association Team GEER Association Report No. GEER-046. http://www.geerassociation.org/.

[2] Sun, J., Hutchinson, T.C., Clahan, K., Menq, F., Lo, E., Chang, W.-J., Tsai, C.-C., Ma, K.-F. with contributions from Hess, M., Kuester, F., Meyer, D., Petrovic, V., and Trinh, S. (2016b). Geotechnical Reconnaissance of the 2016 Mw 6.3 Meinong Earthquake, Taiwan: *Part 2: Remote Sensing Data & Models*. A report of the NSF- Sponsored GEER Association Team GEER Association Report No. GEER-046. http://www.geerassociation.org/.

[3] Wu, Y. M., D.Y. Chen, T. L. Lin, C. Y. Hsieh, T. L. Chin, W. Y. Chang, W. S. Li, and S. H. Ker, 2013. A High-Density Seismic Network for Earthquake Early Warning in Taiwan Based on Low Cost Sensors by Yih-Min Wu, Seismo. Res. Lett., 84, SRL-2013085 1048..1054.

[4] Bray, J., Stewart, J., Baturay, M., Durgunoglu, T., Onalp, A., Sancio, R., Ural, D., Ansal, A., Bardet, J., Barka, A., Boulanger, R., Cetin, O., and Erten, D. (*2000*) Damage Patterns and Foundation Performance in Adapazari. *Earthquake Spectra*: December 2000, Vol. 16, No. S1, pp. 163-189

[5] Coburn, A. and Spence, R. (1992). Earthquake Protection. West Sussex, England. John Wiley & Sons.

[6] Andrus, R. and Stokoe II, K. (2000). "Liquefaction Resistance of Soils from Shear-Wave Velocity." *J. Geotech. Geoenviron. Eng.*, 10.1061/(ASCE)1090-0241(2000)126:11(1015), 1015-1025.

[7] Liquefaction hazard map source: http://map.tgos.tw/TGOSimpleViewer2/Web/Map/TGOSimpleViewer_Map.aspx

[8] 1898 Map source: http://gissrv4.sinica.edu.tw/gis/tainan_en_us.aspx

[9] Meyer, D., Fraijo, E., Lo, E., Rissolo, D., and Kuester, F. (2015). Optimizing UAV Systems for Rapid Survey and Reconstruction of Large Scale Cultural Heritage Sites. *In the Proceedings of the 2nd International Digital Heritage Congress*.

[10] Wittich, C., Hutchinson, T.C., Lo, E., Meyer, D., and Kuester, F. (2014). The South Napa Earthquake of August 24, 2014: Drone-based Aerial and Ground-based LiDAR Imaging Survey. Structural Systems Research Project Report Series. University of California, San Diego. SSRP-2014/09.

[11] Faro (2016). FARO SCENE 5.5. http://www.faro.com/en-us/products/faro-software/scene/overview

[12] Agisoft (2016). Agisoft Photoscan 1.2.3. http://www.agisoft.com/downloads/user-manuals/